Stanford Exploration Project, Report 123, October 31, 2005, pages 25–49

Residual moveout in anisotropic angle-domain common image gathers

Biondo Biondi[1]

ABSTRACT

To enable the analysis of the Residual Moveout (RMO) in Angle-Domain Common Image Gathers (ADCIGs) after anisotropic wavefield-continuation migration, I develop the fundamental concepts for quantitatively relating perturbations in anisotropic parameters to the corresponding reflector movements in ADCIGs. I then apply the general methodology to the particular case of RMO analysis of reflections from flat reflectors in a Vertical Transverse Isotropic (VTI) medium. This analysis shows that the RMO in migrated ADCIGs is a function of both the phase aperture angle and the group aperture angle.

Several numerical examples demonstrate the accuracy of the RMO curves predicted by my kinematic analysis. The synthetic examples also show that the approximation of the group angles by the phase angles may lead to substantial errors for events reflected at wide aperture angles.

The results obtained by migrating a 2-D line extracted from a Gulf of Mexico 3-D data set confirm the accuracy of the proposed method. The RMO curves predicted by the theory exactly match the RMO function observed in the ADCIGs computed from the real data.

INTRODUCTION

The analysis of Residual Moveout (RMO) in Common Image Gathers (CIGs) after prestack migration is an essential step for updating migration velocity. When the migration velocity is inaccurate, the inconsistency of the migrated events along either the offset axis or the aperture-angle axis is proportional to the migration velocity errors. Measuring the RMO in ADCIGs provides the quantitative information necessary to update the velocity function in a Migration Velocity Analysis (MVA) procedure.

Today, MVA is the procedure most commonly employed to estimate isotropic migration velocity in complex media. The technology for anisotropic MVA is much less mature than for isotropic MVA. Recently, important progress has been made toward the development of anisotropic MVA in conjunction with Kirchhoff migration. Sarkar and Tsvankin (2003, 2004b) analyze the effect of velocity errors on offset-domain CIGs produced by Kirchhoff migration. They demonstrate the effectiveness of their method by successfully applying it to a West Africa data set (Sarkar and Tsvankin, 2004a). Krebs et al. (2003) and Bear et al. (2003) integrate

[1]**email:** biondo@sep.stanford.edu

borehole-seismic data and nonseismic information in an MVA process based on Kirchhoff migration.

Wavefield-continuation is capable of producing better images than Kirchhoff migration does in the presence of complex overburden that causes multipathing of the propagating wavefield, as often it occurs when imaging below or in proximity of salt bodies. To perform MVA after wavefield-continuation the RMO function is measured from Angle Domain Common Image Gathers (ADCIGs) (Biondi and Sava, 1999; Clapp and Biondi, 2000). Since all the present methods for computing ADCIGs in conjunction with wavefield migration are limited to isotropic migration, the quantitative analysis of RMO in ADCIGs is also limited to the isotropic case (Biondi and Symes, 2003; Biondi and Tisserant, 2004). In this paper, I provide the basic analytical tools necessary to perform anisotropic migration velocity analysis by analyzing the RMO function in ADCIGs. This paper builds on the results presented in a companion paper (Biondi, 2005) that develops a method for computing ADCIGs after anisotropic migration and lays the foundations for the kinematic analysis of anisotropic ADCIGs. I apply the general theory to the specific case of defining the RMO function measured from flat reflectors in VTI media, because in this case the methodology is simple both to derive and to apply. However, the same concepts could be applied to more general situations, though at the expense of additional complexities that could obfuscate the fundamental concepts.

In (Biondi, 2005) I show that in anisotropic media the ADCIGs are approximately functions of the phase aperture angle, and exactly so for flat reflectors in VTI media. In this paper I demonstrate that the RMO function depends on both the phase and the group aperture angles. This dependency of the RMO function on the group angles adds some complexity to the RMO analysis because the computation of group angles from phase angles, which are measured from the ADCIGs, depends on the background anisotropic velocity evaluated at the reflector point. The synthetic-data examples show that neglecting the dependency on the group angles, and assuming that group angles are equal to phase angles, leads to substantial inaccuracy in the predicted RMO function. Fortunately, the additional computational cost of computing group angles is negligible, and thus it should not be an obstacle to the application of the proposed methodology.

ANGLE-DOMAIN COMMON IMAGE GATHERS AND KINEMATIC ANISOTROPIC MIGRATION

In (Biondi, 2005) I develop the theory of ADCIGs in anisotropic media from both a "plane-wave" viewpoint and a "ray" viewpoint. The two methods are equivalent and yield the same results, but the ray-theoretical approach is the natural starting point for analyzing RMO functions in ADCIGs. The kinematic approach is based on the conceptual generalization of integral (Kirchhoff) migration to the computation of a prestack image that include the sub-surface offset dimension. The image-space of integral migration are usually restricted to the zero subsurface-offset section; that is, with the integral operators (either summation surfaces or spreading surfaces) evaluated when source and receiver rays meet at the reflection point. The image space can be expanded to include non-zero subsurface offsets by integrating the data

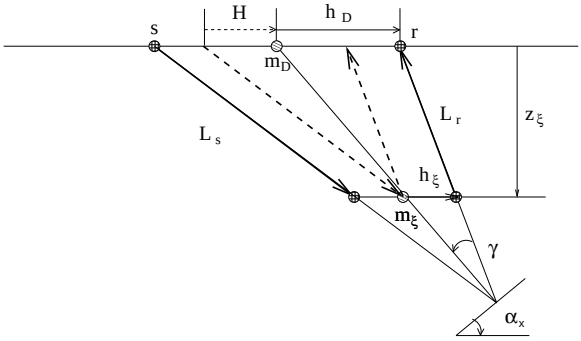

Figure 1: Geometry used for evaluating the impulse response of integral migration generalized to produce a prestack image function of the subsurface offset h_ξ. biondo2-imp-resp [NR]

over surfaces evaluated with the end points of the source and receiver rays horizontally shifted with respect to each other, instead of being coincidental at the image point. Figure 1 illustrates this concept and provide the basis for computing the kinematics of the generalized migration operator.

Since the transformation to ADCIGs operates in the image space, I analyze the spreading surfaces (impulse responses) of the generalized prestack migration operator, which are defined in the image space. In homogeneous anisotropic medium the shape of the impulse responses of the generalized integral migration can be easily evaluated analytically as a function of the subsurface offset h_ξ, in addition to the usual image depth z_ξ and midpoint m_ξ. Figure 1 illustrates the geometry used to evaluate this impulse response.

Assuming an arbitrary homogeneous anisotropic medium, simple trigonometry applied to Figure 1 allows us to express the impulse response in parametric form, as a function of the group dip angle α_x and the group aperture angle γ. If we migrate an impulse recorded at time t_D, midpoint m_D and surface offset h_D, the migration impulse response can be expressed as follows:

$$z_\xi = L(\alpha_x,\gamma)\frac{\cos^2\alpha_x-\sin^2\gamma}{\cos\alpha_x\cos\gamma}, \tag{1}$$

$$m_\xi = m_D - L(\alpha_x,\gamma)\frac{\sin\alpha_x}{\cos\gamma}, \tag{2}$$

$$h_\xi = h_D - H = h_D - L(\alpha_x,\gamma)\frac{\sin\gamma}{\cos\alpha_x}, \tag{3}$$

with the average half-path length $L(\alpha_x,\gamma)$ given by:

$$L(\alpha_x,\gamma) = \frac{L_s+L_r}{2} = \frac{t_D}{(S_r+S_s)+(S_r-S_s)\tan\alpha_x\tan\gamma}, \tag{4}$$

where S_s and S_r are the group slowness along the source and receiver rays, respectively.

In 2-D, The ADCIGs are computed by applying a slant-stack decomposition on the prestack image along the subsurface offset axis, at constant midpoint. The kinematics of the transfor-

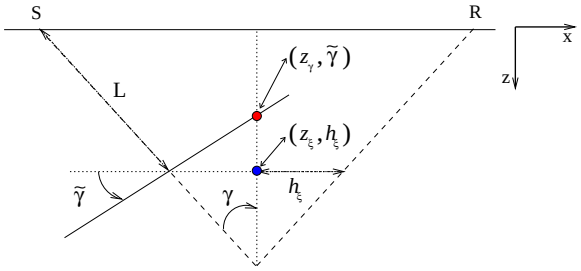

Figure 2: Geometry of the transformation to the angle domain. The image point in the subsurface-offset domain (z_ξ, h_ξ) moves to the image point in angle domain $(z_\gamma, \widetilde{\gamma})$. biondo2-cig-2d-aniso-mva-flat-v1 [NR]

mation are defined by the following change of variables:

$$\widehat{\gamma} = \arctan \left. \frac{\partial z_\xi}{\partial h_\xi} \right|_{m_\xi = \overline{m}_\xi}, \tag{5}$$

$$z_\gamma = z_\xi - h_\xi \left. \frac{\partial z_\xi}{\partial h_\xi} \right|_{m_\xi = \overline{m}_\xi}, \tag{6}$$

where z_γ is the depth of the image point after the transformation. In the general case, the angle $\widehat{\gamma}$ is related to the reflection aperture angle in a non-trivial way. However, in (Biondi, 2005) I demonstrate that for flat reflectors the slope of the impulse response along the subsurface offset axis, is equal to the tangent of the phase aperture angle $\widetilde{\gamma}$; that is,

$$\left. \frac{\partial z_\xi}{\partial h_\xi} \right|_{(m_\xi = \overline{m}_\xi,\, \alpha_x = 0)} = \frac{\tan\gamma + \frac{1}{S}\frac{\partial S}{\partial \gamma}}{1 - \frac{1}{S}\frac{\partial S}{\partial \gamma}\tan\gamma} = \tan\widetilde{\gamma}. \tag{7}$$

Notice that throughout this paper I use the tilde symbol to distinguish between phase quantities (with a tilde) and group quantities (without a tilde). Appendix A summarizes the relationships between group angles and velocities and phase angles and velocities. Equation A-4 is directly used to derive the result in equation 7.

Substituting equation 7 in equations 5 and 6 we obtain

$$\widetilde{\gamma} = \arctan \left. \frac{\partial z_\xi}{\partial h_\xi} \right|_{m_\xi = \overline{m}_\xi}, \tag{8}$$

$$z_\gamma = z_\xi - h_\xi \tan\widetilde{\gamma}. \tag{9}$$

Figure 2 provides a geometrical interpretation of the transformation to angle domain of an image point with non-zero subsurface offset. The transformation to angle domain moves the image point in the subsurface-offset domain (z_ξ, h_ξ) to the image point in angle domain $(z_\gamma, \widetilde{\gamma})$. The depth of the image point in angle domain is determined by the intersection of the lines passing through the points $(z_\xi, m_\xi \pm h_\xi)$ and tilted by $\mp\widetilde{\gamma}$ with respect to the horizontal. When the migration velocity is correct, and the image is fully focused at zero subsurface offset, the transformation to angle domain does not change the depth of the image point and the reflections are imaged at the same depth for all aperture angles. On the contrary, when the reflections are not focused at zero offset, the transformation to angle domain maps the events at different depths for each different angle. The variability of the depth z_γ with the aperture angle is described by the RMO function that we want to measure and quantify as a function of the perturbations in anisotropic parameters encountered along the propagation paths.

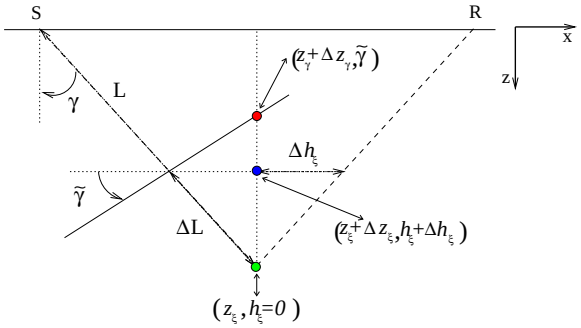

Figure 3: Linearized perturbations of the image-point locations (both in the subsurface-offset domain and the angle domain) caused by changes in the ray length L, as evaluated using the first term in equation 11. biondo2-cig-2d-aniso-delta1-flat-v1 [NR]

ANISOTROPIC RESIDUAL MOVEOUT FOR FLAT REFLECTORS

The generalization of kinematic anisotropic migration and the analysis of the kinematics of the offset-to-angle transformation presented in the previous section enables a simple analysis of the residual moveout (RMO) in ADCIGs caused by errors in anisotropic velocity parameters. In this section I derive the RMO function by linearizing the relationship of the imaging depth in the angle domain with respect to perturbations in the anisotropic parameters. The linearization is evaluated around the correct migration velocity function; that is, when the image in the subsurface-offset domain is well focused at zero offset.

As in the previous section, I limit my analysis to reflections from flat interfaces. However, a generalization of the flat-events analysis to dipping events should be conceptually straightforward, though not necessarily simple from the analytical point of view. Furthermore, I derive relationships assuming that the velocity perturbations are limited to a homogeneous half-space above the reflector. The same relationships can be easily adapted to the case of a homogeneous layer above the reflector by transforming the depth variable into a relative depth with respect to the top of the layer under consideration. At the end of this section I present the fundamental relationship for broadening the application of the theory to heterogeneous media. This relationship links the traveltime perturbations to the reflector movements and it can be used in a ray-based tomographic velocity-update procedure.

A VTI velocity function, either group or phase, is described by the following vector of three velocities $\mathbf{V} = (V_V, V_H, V_N)$, or by the corresponding vector of three slownesses $\mathbf{S} = (S_V, S_H, S_N)$ used in equation C-1. I define the perturbations as the combination of one multiplicative factor for each of the velocities and one multiplicative factor for all velocities; that is, the perturbed velocity ${}_\rho\mathbf{V}$ is defined as:

$$ {}_\rho\mathbf{V} = \left({}_\rho V_V, {}_\rho V_H, {}_\rho V_N\right) = \rho_V \left(\rho_{V_V} V_V, \rho_{V_H} V_H, \rho_{V_N} V_N\right). \tag{10}$$

The velocity-parameter perturbations is thus defined by the following four-components vector $\boldsymbol{\rho} = \left(\rho_V, \rho_{V_V}, \rho_{V_H}, \rho_{V_N}\right)$.

Differentiating, the expression for the depth of the image point in the angle domain z_γ (equation 9) with respect to the i-th component in the perturbation vector, we obtain the fol-

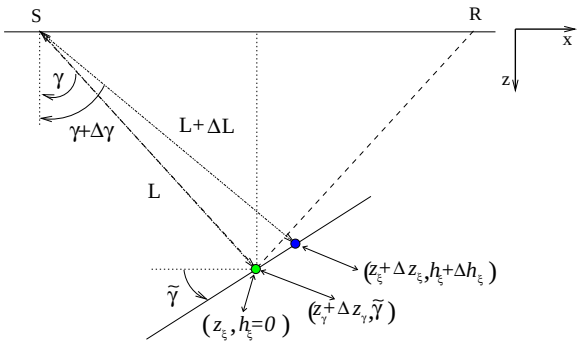

Figure 4: Linearized perturbations of the image-point locations (both in the subsurface-offset domain and the angle domain) caused by changes in the aperture angle γ, as evaluated using the second term in equation 11. Notice that the image point in the angle domain does not move, no matter how large the corresponding movement in the subsurface-offset domain is. biondo2-cig-2d-aniso-delta2-flat-v1 [NR]

lowing:

$$\frac{\partial z_\gamma}{\partial \rho_i} = \frac{\partial z_\gamma}{\partial L}\frac{\partial L}{\partial \rho_i} + \frac{\partial z_\gamma}{\partial \gamma}\frac{\partial \gamma}{\partial \rho_i} + \frac{\partial z_\gamma}{\partial \widetilde{\gamma}}\frac{\partial \widetilde{\gamma}}{\partial \rho_i} \tag{11}$$

$$= \frac{\partial z_\gamma}{\partial L}\frac{\partial L}{\partial S}\left(\frac{\partial S}{\partial \rho_i} + \frac{\partial S}{\partial \gamma}\frac{\partial \gamma}{\partial \rho_i}\right) + \frac{\partial z_\gamma}{\partial \gamma}\frac{\partial \gamma}{\partial \rho_i} + \frac{\partial z_\gamma}{\partial \widetilde{\gamma}}\frac{\partial \widetilde{\gamma}}{\partial \rho_i} \tag{12}$$

$$= \frac{\partial z_\gamma}{\partial L}\frac{\partial L}{\partial S}\frac{\partial S}{\partial \rho_i} + \left(\frac{\partial z_\gamma}{\partial L}\frac{\partial L}{\partial S}\frac{\partial S}{\partial \gamma} + \frac{\partial z_\gamma}{\partial \gamma}\right)\frac{\partial \gamma}{\partial \rho_i} + \frac{\partial z_\gamma}{\partial \widetilde{\gamma}}\frac{\partial \widetilde{\gamma}}{\partial \rho_i}. \tag{13}$$

In Appendix B I demonstrate that the terms multiplying the partial derivatives with respect to the angles are zero, and equation 13 simplifies into:

$$\frac{\partial z_\gamma}{\partial \rho_i} = \frac{\partial z_\gamma}{\partial L}\frac{\partial L}{\partial S}\frac{\partial S}{\partial \rho_i}, \tag{14}$$

where

$$\frac{\partial z_\gamma}{\partial L} = \frac{\partial z_\xi}{\partial L} - \frac{\partial h_\xi}{\partial L}\tan\widetilde{\gamma} = \cos\gamma + \sin\gamma\tan\widetilde{\gamma}, \tag{15}$$

and

$$\frac{\partial L}{\partial S(\gamma)} = -\frac{z_\xi}{S(\gamma)\cos\gamma}, \tag{16}$$

and consequently

$$\frac{\partial z_\xi}{\partial \rho_i} = -\frac{z_\gamma\,(1+\tan\gamma\tan\widetilde{\gamma})}{S(\gamma)}\frac{\partial S}{\partial \rho_i}. \tag{17}$$

Figures 3 and 4 graphically illustrate the image perturbations related to the first two terms in equation 11. Figure 3 shows the movement of the image points (both in the subsurface-offset domain and the angle domain) caused by changes in the ray length L. Figure 4 provides

a geometrical explanation of why the second term in equation 11 vanishes. It shows that perturbations in the aperture angle γ cause the subsurface-offset domain image point to move along the tangent to the wavefront (tilted with the phase angle $\widetilde{\gamma}$). Since this movement is constrained along the tangent, the image point in the angle domain does not move, no matter how large the movement in the subsurface-offset domain is.

RMO function with uniform scaling of velocity

In case of uniform scaling of velocity, the derivative of the imaging depth z_γ with respect to the perturbation component ρ_V has the following simple form:

$$\frac{\partial z_\gamma}{\partial \rho_V} = z_\xi \, (1 + \tan\gamma \tan\widetilde{\gamma}), \tag{18}$$

because the derivative of the slowness with respect to a uniform scaling of the velocity has the following simple form:

$$\frac{\partial S(\gamma)}{\partial \rho_V} = -S(\gamma), \tag{19}$$

that causes the derivative $\partial L / \partial \rho_V = -z_\xi / \cos\gamma$ to be independent from the "local" shape of the anisotropic slowness function. Intuitively, this simplification is related to the fact that the "shape" of the wavefronts is not affected by a uniform scaling of the velocity.

The residual moveout Δz_{RMO} is defined as the difference between the reflector movement at finite aperture angle $\widetilde{\gamma}$ and the reflector movement at normal incidence. From equation 18 the partial derivative of Δz_{RMO} with respect to ρ_V is equal to the following expression:

$$\frac{\partial \Delta z_{\mathrm{RMO}}}{\partial \rho_V} = z_\xi \tan\gamma \tan\widetilde{\gamma}. \tag{20}$$

When the medium is isotropic, and the phase angles are equal to the group angles, the RMO expression in equation 20 becomes the RMO expression introduced by Biondi and Symes (2003).

The dependency of equation 20 from the group angles increases the complexity of its use because it requires the transformation of phase angles (measured directly from the ADCIGs) into group angles by applying equation A-2. The computational cost of evaluating equation A-2 is negligible, but its use makes the computations dependent on the local values of the background anisotropic velocity function. On the other hand, the following numerical examples show that substantial errors are introduced when the distinction between the group and phase angles is neglected, and the phase angle is used instead of the group angle in equation 20.

RMO function with arbitrary scaling of velocity

The expressions of the derivative of z_γ with respect to arbitrary perturbations of individual velocity components (i.e. V_V, V_H, and V_N) are slightly more complex than with respect to ρ_V

because the wavefronts are deformed when the velocity components are unevenly perturbed. These derivatives can be expressed as:

$$\frac{\partial z_\gamma}{\partial \rho_{V_V}} = -\frac{z_\xi}{S(\gamma)}\frac{\partial S(\gamma)}{\partial \rho_{V_V}}(1+\tan\gamma\tan\widetilde{\gamma}), \tag{21}$$

$$\frac{\partial z_\gamma}{\partial \rho_{V_H}} = -\frac{z_\xi}{S(\gamma)}\frac{\partial S(\gamma)}{\partial \rho_{V_H}}(1+\tan\gamma\tan\widetilde{\gamma}), \tag{22}$$

$$\frac{\partial z_\gamma}{\partial \rho_{V_N}}, = -\frac{z_\xi}{S(\gamma)}\frac{\partial S(\gamma)}{\partial \rho_{V_N}}(1+\tan\gamma\tan\widetilde{\gamma}). \tag{23}$$

The partial derivatives of the RMO function Δz_{RMO} are directly derived from the partial derivatives of z_γ, taking into account that for flat reflectors only the vertical velocity component V_V influences the image depth of normal incidence. The derivatives of Δz_{RMO} can thus be written as follows:

$$\frac{\partial \Delta z_{\text{RMO}}}{\partial \rho_{V_V}} = -\frac{z_\xi}{S(\gamma)}\frac{\partial S(\gamma)}{\partial \rho_{V_V}}(1+\tan\gamma\tan\widetilde{\gamma}) - z_\xi, \tag{24}$$

$$\frac{\partial \Delta z_{\text{RMO}}}{\partial \rho_{V_H}} = -\frac{z_\xi}{S(\gamma)}\frac{\partial S(\gamma)}{\partial \rho_{V_H}}(1+\tan\gamma\tan\widetilde{\gamma}), \tag{25}$$

$$\frac{\partial \Delta z_{\text{RMO}}}{\partial \rho_{V_N}} = -\frac{z_\xi}{S(\gamma)}\frac{\partial S(\gamma)}{\partial \rho_{V_N}}(1+\tan\gamma\tan\widetilde{\gamma}). \tag{26}$$

The expressions for the derivatives of the slowness function with respect to the perturbation parameters depend on the particular form chosen to approximate the slowness function. Appendix C presents a particular approximation to the VTI group slowness function and derives the corresponding partial derivatives to be substituted in equations 21–23 and in equations 24–26. I used the same approximation to the VTI group slowness for the numerical experiments shown in this paper.

Conversion of depth errors into traveltime errors in heterogeneous media

The RMO functions derived above can be directly used in a layered-based vertical updating of the velocity function after migration. However, in complex media it is often desirable to invert the depth errors measured from ADCIGs into velocity-parameter perturbations through a tomographic procedure. To be able to apply a tomographic method, we must perform an additional step to convert the depth errors measured from ADCIGs into traveltime errors. This depth-to-time conversion can be easily accomplished by slightly rewriting the chain of partial derivatives in equation 14, and obtain the following relationship:

$$\frac{\partial z_\gamma}{\partial t} = \frac{\partial z_\gamma}{\partial L}\frac{\partial L}{\partial t} = \frac{\cos\gamma + \sin\gamma\tan\widetilde{\gamma}}{S(\gamma)}, \tag{27}$$

which can be directly applied to convert depth errors into traveltime perturbations to be used in tomography.

It is immediate to verify that in the isotropic case, in which $\widetilde{\gamma} = \gamma$, equation 27 simplifies into the following relationship:

$$\frac{\partial z_\gamma}{\partial t} = \frac{1}{\cos\gamma\, S(\gamma)}, \tag{28}$$

which is equivalent to the relationship derived for isotropic MVA by Biondi and Symes (2003).

Synthetic-data examples of RMO function in ADCIGs

To verify the accuracy of the RMO functions derived in this section I performed several numerical tests using synthetic data modeled and migrated using an anisotropic source-receiver migration and modeling program. This program performed depth extrapolation by numerically solving the following dispersion relation:

$$k_z = \frac{\omega}{V_V}\sqrt{\frac{\omega^2 - {V_H}^2 k_x^2}{\omega^2 + \left({V_N}^2 - {V_H}^2\right) k_x^2}}, \tag{29}$$

where ω is the temporal frequency, and k_x and k_z are respectively the horizontal and vertical wavenumbers. This dispersion relation corresponds to the slowness functions in equation C-1 (Fowler, 2003), which was used to compute the RMO functions according to the theory developed above.

To test the theory under realistic and diverse anisotropic conditions, in the numerical examples I used three sets of anisotropic Thomsen parameters representing three different rocks described by Tsvankin (2001):

- Taylor Sand : $\epsilon = 0.110\ \ \delta = -0.035,\ \ \rightarrow \eta = .155,$
- Mesa Clay Shale : $\epsilon = 0.189,\ \ \delta = 0.204 \rightarrow \eta = -.010,$
- GreenLight River Shale : $\epsilon = 0.0975,\ \ \delta = -0.11,\ \ \rightarrow \eta = .266.$

The GreenLight River Shale is derived from the Green River Shale described by Tsvankin (2001) by halving the anisotropic parameters (ϵ and δ), because the strong anelliptic nature of the original one ($\eta = .74$) causes the group-slowness approximation in equation C-1 to break down. Consequently, the kinematic computations based on ray tracing, and thus on group velocity and angles, become inconsistent with wavefield migration based on the dispersion relation in equation 29. Notice that the GreenLight River Shale is still the most anelliptic among the set of rocks I am using.

The first set of numerical experiments tests the RMO equation with uniform scaling of velocity expressed in equation 20. In addition to the three anisotropic cases described above, this RMO function is tested also for the special case of isotropic velocity. The second set tests the generalized RMO functions expressed in equations 24–26. Only the three anisotropic cases are tested because there is no meaningful isotropic case to test the generalized RMO function. In all the synthetic-data examples I plot the correct RMO curve computed by applying either equation 18 or equations 24–26, and the approximate RMO curve computed using

an "isotropic" approximation and ignoring the distinction between the group aperture angle γ and the phase aperture angle $\widetilde{\gamma}$.

Figure 5 shows ADCIGs when an anisotropic velocity was perturbed by $\rho_V = .99$. The four panels correspond to four rock types: a) Isotropic, b) Taylor Sand, c) Mesa Clay Shale, and d) GreenLight River Shale. Superimposed onto the images are the RMO functions computed using equation 20. The solid line was computed by computing $\tan\gamma$ from $\tan\widetilde{\gamma}$ by applying equation A-2, whereas the dashed line was computed by approximating $\tan\gamma$ as equal to $\tan\widetilde{\gamma}$. The RMO curves computed using the correct group angle perfectly match the residual moveout of the images. On the contrary, when the phase angles are used instead of the group angles, significant errors are introduced even for such a small perturbation in the parameters ($\rho_V = .99$). It is interesting to notice that the errors are larger for the rock types exhibiting strong anelliptic anisotropy (Taylors Sand and GreenLight River Shale) than for the strongly anisotropic but quasi-elliptical rock (Mesa Clay Shale).

The expression for the RMO function derived in equation 20 is based on a linearization, and thus when the perturbations in velocity parameters are large it is not as accurate as it is when the perturbations are small (e.g. $\rho_V = .99$). Figure 6 illustrates this fact by showing a similar experiment as the one shown in Figure 5, but with a perturbation 10 times larger; that is, with $\rho_V = .9$. As in Figure 5, the four panels correspond to four rock types: a) Isotropic, b) Taylor Sand, c) Mesa Clay Shale, and d) GreenLight River Shale, and the lines superimposed onto the images are the RMO functions computed by using the correct values for $\tan\gamma$ (solid lines), and by using $\tan\widetilde{\gamma}$ in place of $\tan\gamma$ (dashed lines). With large perturbations, the predicted RMO functions differ from the actual RMO functions at wide aperture angles even when the correct values of the group angles are used in equation 20. However, even with such large perturbations the predicted RMO functions are still useful approximations of the actual RMO functions. In particular, it can be observed that the predicted RMO function correctly approximates the differences in shape of the actual RMO function among the rock types. These shape variations are related to the variations in shape of the wavefronts, which are reflected in the predicted RMO function through the variations in the mapping from phase angles to group angles. Figures 7 and 8 show examples of the application of the generalized RMO functions expressed in equations 24–26. As in Figures 5–6, I show the ADCIGs for three different anisotropic rock types, but, differently from the previous figures, not for the isotropic case. The order of the rock types is the same as in Figures 5–6; that is: panels a) correspond to Taylor Sand, panels b) to Mesa Clay Shale, and panels c) to GreenLight River Shale. Furthermore, as in Figures 5–6, one figure (Figure 8) shows the ADCIG obtained with a smaller perturbation than the ADCIGs shown in the other figure (Figure 7). The ADCIGs shown in Figure 7 were obtained by performing *isotropic* migration on the synthetic data modeled assuming *anisotropic* velocity. The ADCIGs shown in Figure 8 were computed by scaling by .25 the parameter perturbations used to compute Figure 7. The lines superimposed onto the images are the RMO functions computed by using the correct values for $\tan\gamma$ (solid lines), and by using $\tan\widetilde{\gamma}$ in place of $\tan\gamma$ (dashed lines).

The predicted RMO functions accurately track the actual RMO functions when the parameter perturbations are sufficiently small to be within the range of accuracy of the linearization at the basis of the derivation of equation 20 (Figure 8). But even when the perturbations are

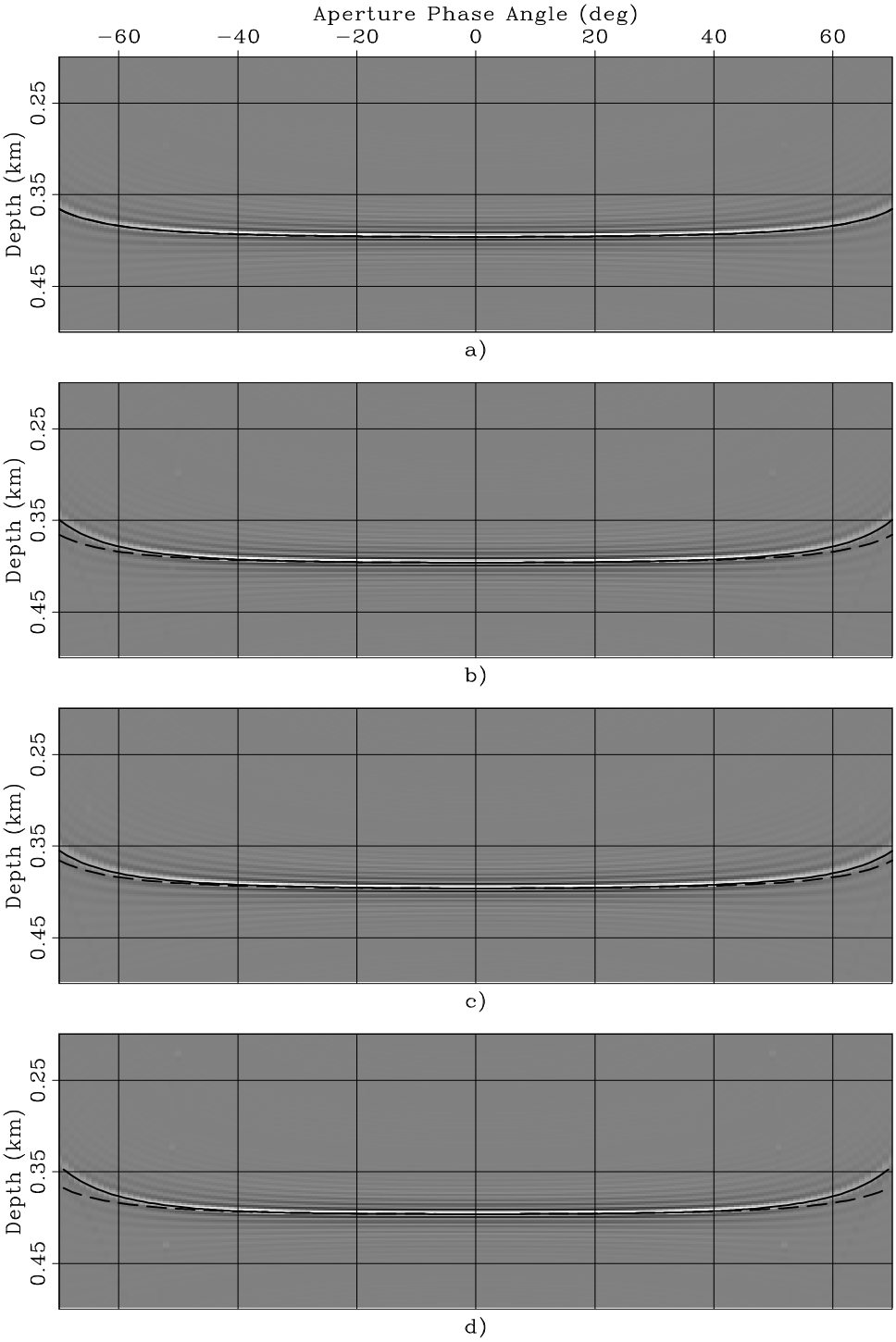

Figure 5: ADCIGs obtained when a constant anisotropic velocity was perturbed by $\rho_V = .99$ for four rock types: a) Isotropic, b) Taylor Sand, c) Mesa Clay Shale, and d) GreenLight River Shale. Superimposed onto the images are the RMO functions computed using equation 20. The solid line was computed when $\tan\gamma$ was derived from $\tan\widetilde{\gamma}$ by applying equation A-2, whereas the dashed line was computed by approximating $\tan\gamma$ as equal to $\tan\widetilde{\gamma}$. biondo2-Quad_Aniso-rho.99_overn [CR]

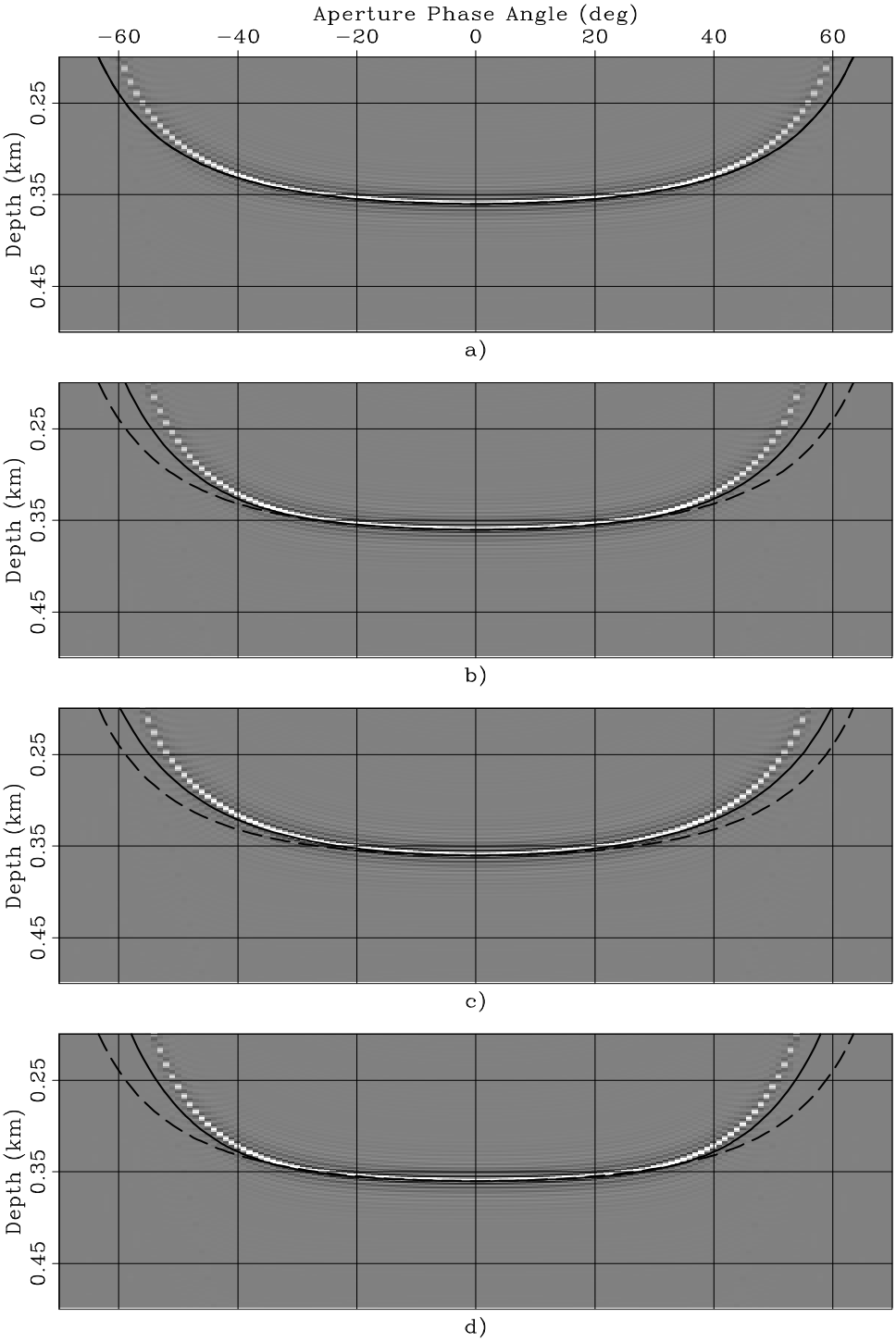

Figure 6: ADCIGs obtained when a constant anisotropic velocity was perturbed by $\rho_V = .9$ for four rock types: a) Isotropic, b) Taylor Sand, c) Mesa Clay Shale, and d) GreenLight River Shale. Superimposed onto the images are the RMO functions computed using equation 20. The solid line was computed when $\tan\gamma$ was derived from $\tan\widetilde{\gamma}$ by applying equation A-2, whereas the dashed line was computed by approximating $\tan\gamma$ as equal to $\tan\widetilde{\gamma}$. biondo2-Quad_Aniso-rho.9_overn [CR]

large (Figure 7) and cause a substantial RMO (up to 30% of the reflector depth) the predicted RMO functions are excellent approximations of the actual RMO functions.

The RMO functions associated with the two strongly anelliptic rocks (Taylor Sand and GreenLight River Shale) exhibit a characteristic oscillatory behavior; the events at narrow-aperture angles are imaged deeper than the normal incidence event, whereas the events at wide-aperture angles are imaged shallower. This oscillatory behavior is well predicted by the analytical RMO function introduced in equations 24–26.

In contrast, the approximation of the group angles with the phase angles (dashed lines in the figures) seriously deteriorates the accuracy of the predicted RMO functions. Notice that, in contrast with the uniform-perturbation case illustrated in Figures 5– 6, the dashed lines are different among the panels, because the derivatives of the slowness function with respect to the perturbation parameters depend on the anisotropic parameters of the background medium.

GULF OF MEXICO DATA EXAMPLE

To test the accuracy of the RMO functions derived in this paper, I migrated a 2-D line extracted from a 3-D data set that was kindly provided to SEP by ExxonMobil. To minimize 3-D effects, the location of the 2-D line was chosen in an area where the sediments are mostly flat in the cross-line direction and where the salt flanks are mostly perpendicular to the in-line direction.

The data set was acquired in the Gulf of Mexico over an existing reservoir. Therefore several borehole seismic data sets were available in addition to the surface data to constraint the estimation of the anisotropic parameters. ExxonMobil provided SEP with three anisotropic-parameter cubes resulting from a joint inversion of the surface data and the borehole data (Krebs et al., 2003). Figure 9 shows the vertical slices cut through these cubes at the cross-line location corresponding to the 2-D line that I migrated. Panel a) displays the vertical velocity, panel b) displays the values of δ, and panel c) displays the values of η. To avoid artifacts caused by sharp parameter contrasts, for migration I removed the salt body from the functions displayed in Figure 9. I "infilled" the salt body with sediment-like values by interpolating the functions inward starting from the sediment values at the salt-sediment interface.

Figure 10 compares the result of anisotropic prestack depth migration (panel a) with the results of isotropic depth migration obtained using as migration velocity the vertical velocity function (panel b). The anisotropic-migration image is clearly superior to the isotropic-migration image that shows clear sign of undermigration of the salt-flanks reflections as well of the sediments terminating against the salt body. All the reflectors are nicely imaged by the anisotropic migration, except for the shallow tract of the salt flank on the left-hand side of the body because it has large cross-line dip components.

Figure 11 shows two examples of ADCIGs computed from both the anisotropic and the isotropic migration results. The CIGs shown in panel a) and b) are taken at surface location of 3,725 meters (left vertical black line in Figure 10) and the CIGs shown in panel c) and d) are taken at surface location of 11,625 meters (right vertical black line in Figure 10). The

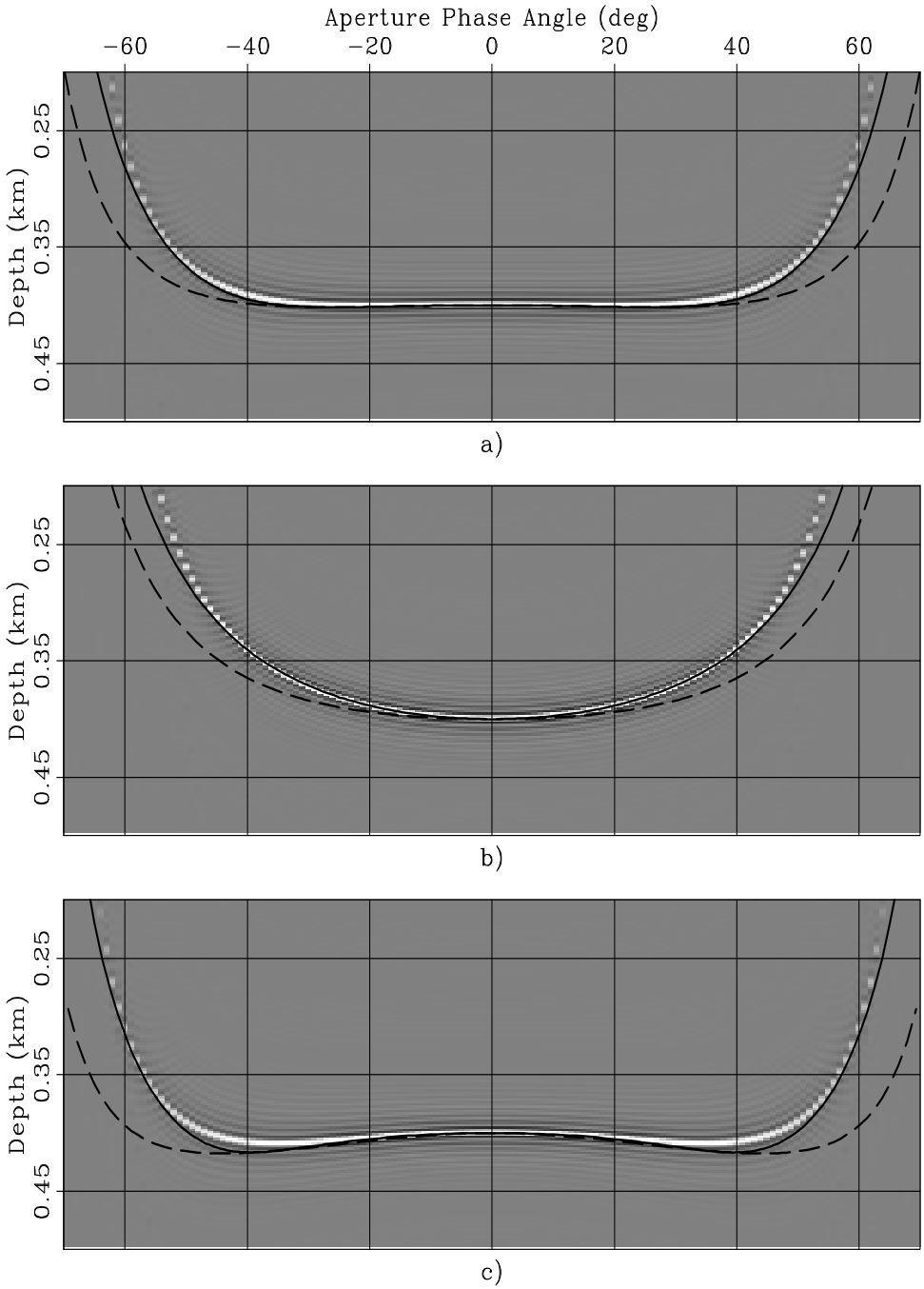

Figure 7: ADCIGs obtained when data modeled with an *anisotropic* velocity have been migrated using an *isotropic* velocity. The anisotropic data were modeled assuming three rock types: a) Taylor Sand, b) Mesa Clay Shale, and c) GreenLight River Shale. Superimposed onto the images are the RMO functions computed using equation 20. The solid line was computed when $\tan\gamma$ was derived from $\tan\widetilde{\gamma}$ by applying equation A-2, whereas the dashed line was computed by approximating $\tan\gamma$ as equal to $\tan\widetilde{\gamma}$. biondo2-Trio_Aniso-iso_overn [CR]

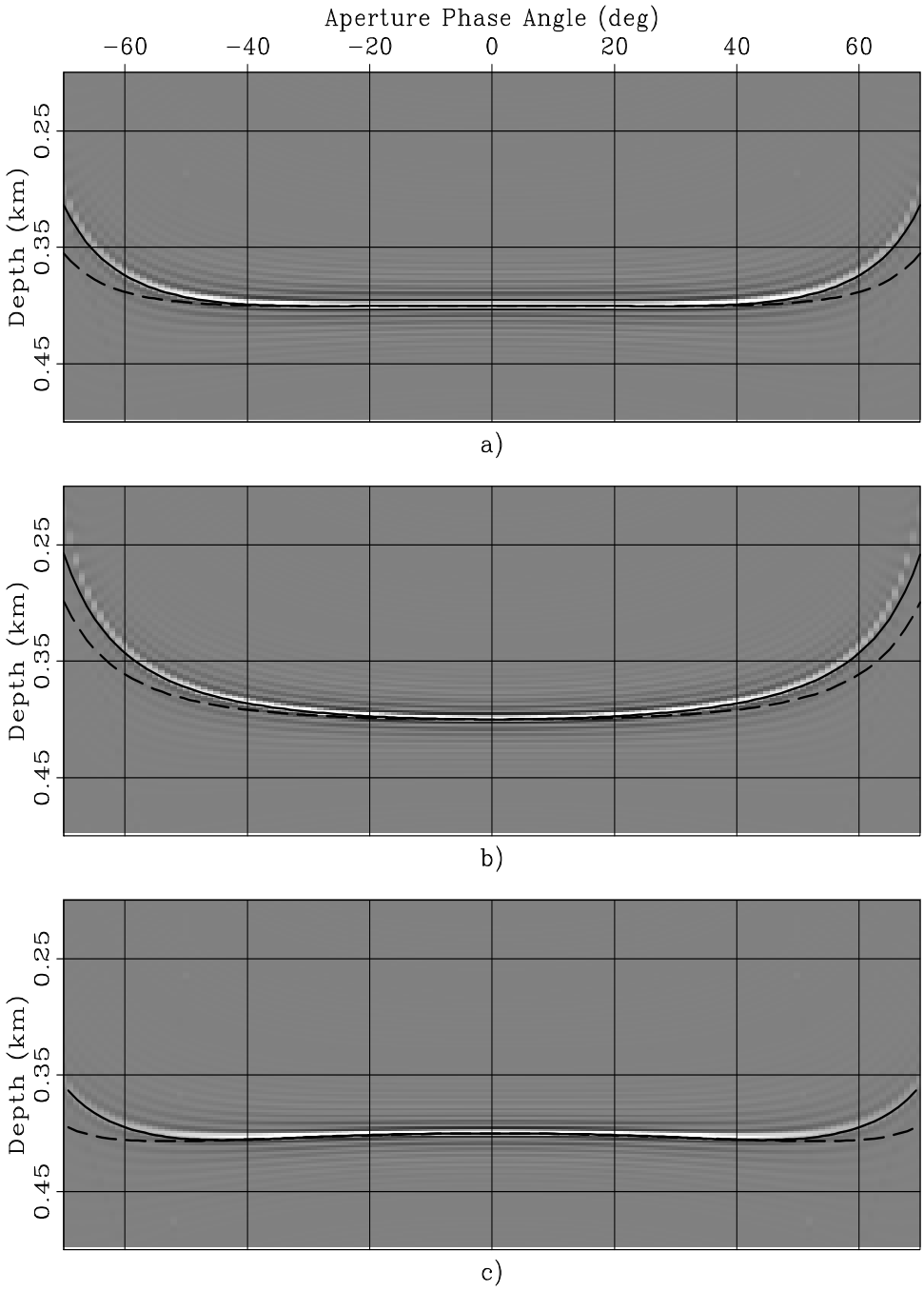

Figure 8: ADCIGs obtained when data modeled with an *anisotropic* velocity have been migrated using a *less anisotropic* velocity; that is, with anisotropic parameters obtained by scaling by .25 the parameter perturbations used to compute Figure 7. The anisotropic data were modeled assuming three rock types: a) Taylor Sand, b) Mesa Clay Shale, and c) GreenLight River Shale. Superimposed onto the images are the RMO functions computed using equation 20. The solid line was computed when $\tan\gamma$ was derived from $\tan\widetilde{\gamma}$ by applying equation A-2, whereas the dashed line was computed by approximating $\tan\gamma$ as equal to $\tan\widetilde{\gamma}$. biondo2-Trio_Aniso-scaled_overn [CR]

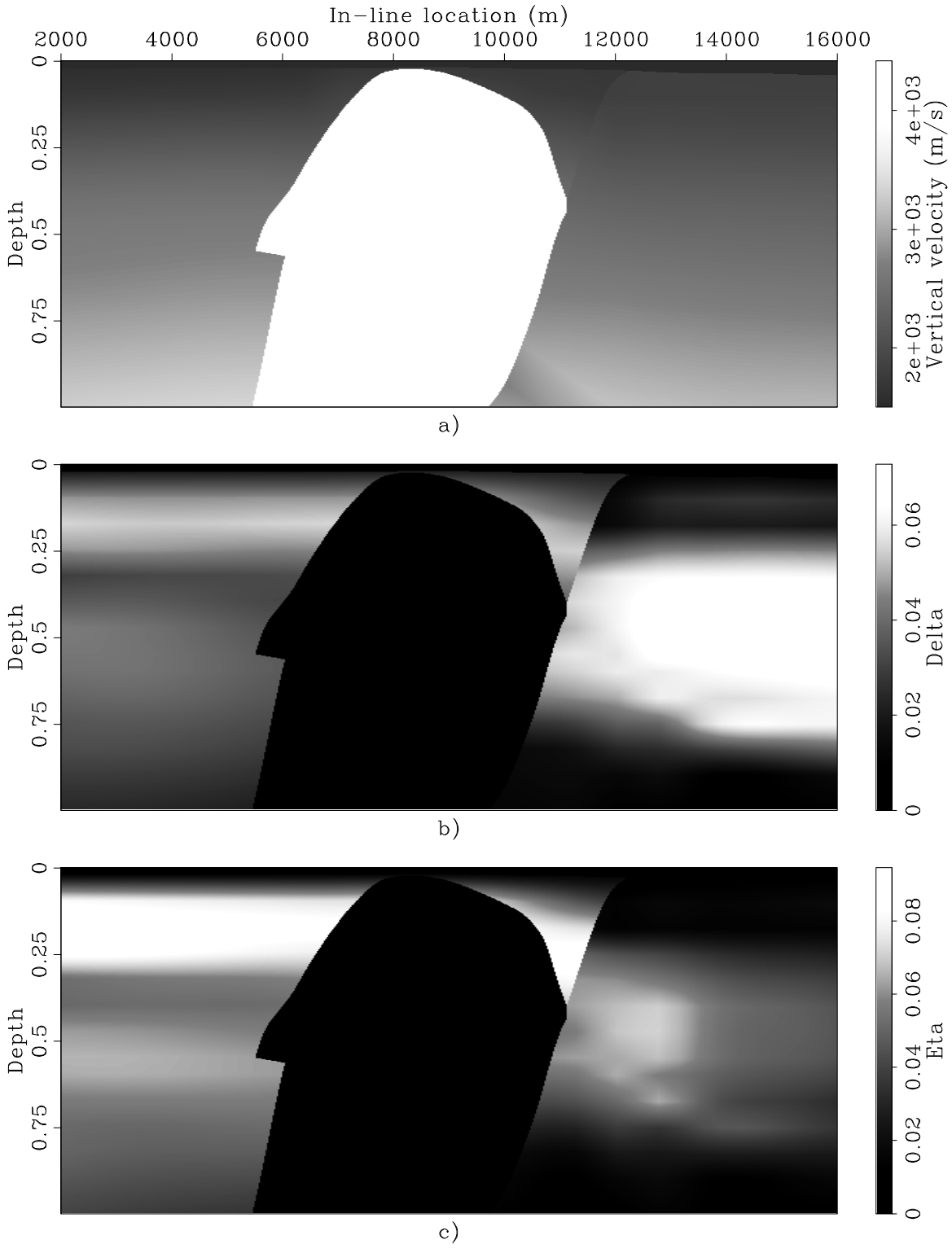

Figure 9: Vertical slices cut through the anisotropic velocity parameters cubes. Panel a) shows the vertical velocity field, panel b) shows the δ field, and panel c) shows the η field. I removed the salt body from the parameters functions used for migration, to avoid artifacts caused by sharp parameter discontinuities. biondo2-Par-Sections-overn [CR]

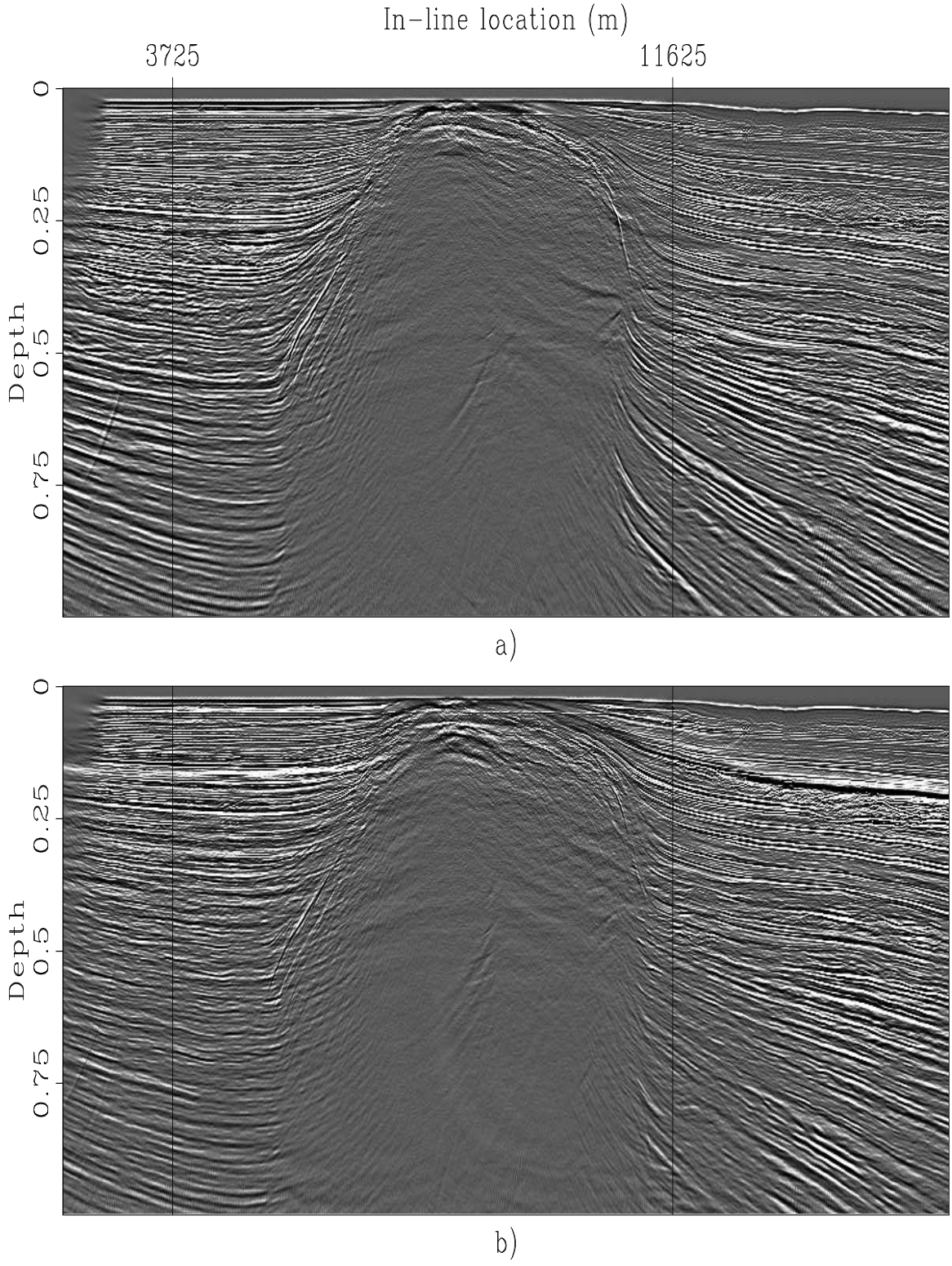

Figure 10: Images obtained by anisotropic prestack migration (panel a) and isotropic prestack migration (panel b). The two vertical lines superimposed onto the image identify the surface location of the ADCIGs displayed in Figure 11. biondo2-Sections-overn [CR]

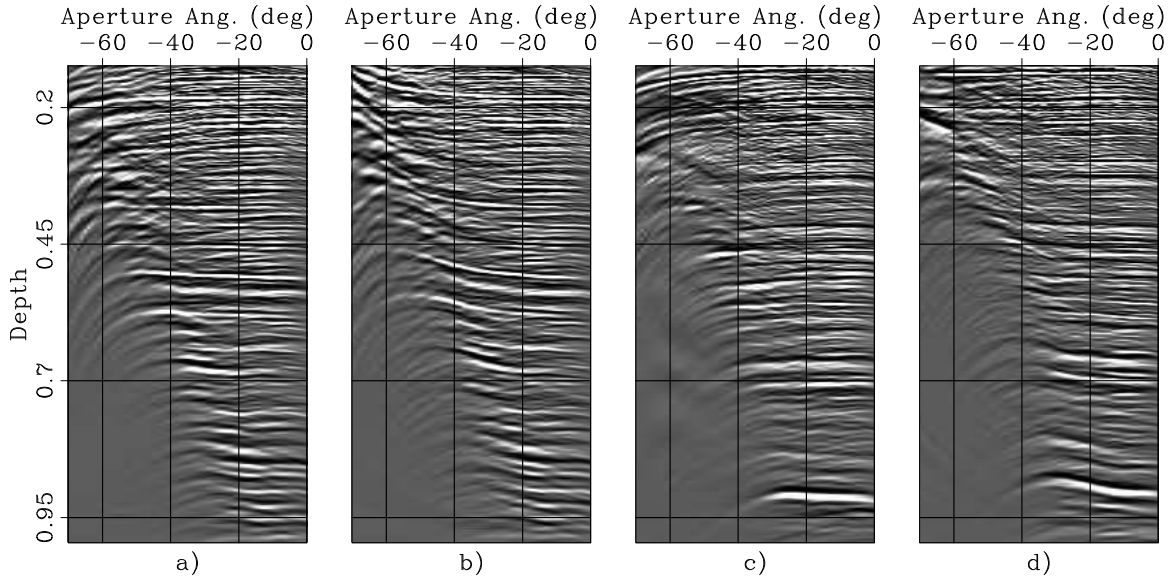

Figure 11: ADCIGs computed by anisotropic migration (panels a) and c)) and isotropic migration (panels b) and d)). The ADCIG shown in panels a) and b) are taken at the surface location of 3,725 meters. The ADCIG shown in panel c) and d) are taken at the surface location of 11,625 meters. biondo2-Quad-aniso-iso-overn [CR]

ADCIGs obtained by anisotropic migration (panels a and c) are uniformly flatter than the ADCIGs obtained by isotropic migration (panels b and d). The ADCIGs obtained by isotropic migration display the typical hockey-stick behavior commonly seen in CIGs computed by isotropic Kirchoff migration in anisotropic media. Although the isotropic migration image is evidently not well focused, this result does not preclude the possibility that an isotropic migration velocity could be defined to focus the data satisfactorily. However, an isotropic migration with a different velocity model would also position the reflectors at substantially different locations. These location would not equally match the depth measured from the wells (Bear et al., 2003).

The RMO function derived in this paper assumes a homogeneous layer above the reflector to be analyzed. To test the accuracy of the expressions for the RMO function I therefore estimated the average anisotropic parameters between the sea floor and two reflectors, one shallow and the other deep, easily identifiable in the ADCIG located at 3,725 meters (Figure 11a). Figures 12 and 13 show the result of my analysis.

Figure 12c shows the ADCIG obtained after anisotropic migration using the following average parameters below the sea floor: $V_V = 1,750$ m/s, $\epsilon = 0.11$, $\delta = 0.04$, and $\eta = .065$. Figure 12d shows the ADCIG obtained after isotropic migration using $V_V = 1,750$ m/s. The shallow reflection of interest is flat in Figure 12c, whereas it is smiling upward in Figure 12d. For comparison, Figures 12a and 12b show a zoom of Figures 11a and 11b into the same window of the ADCIGs as the one displayed in Figures 12c and 12d. The curve superimposed onto both Figures 12b and 12d was computed using the generalized RMO functions expressed in equations 24–26. The computed RMO function perfectly overlaps the event in the ADCIG

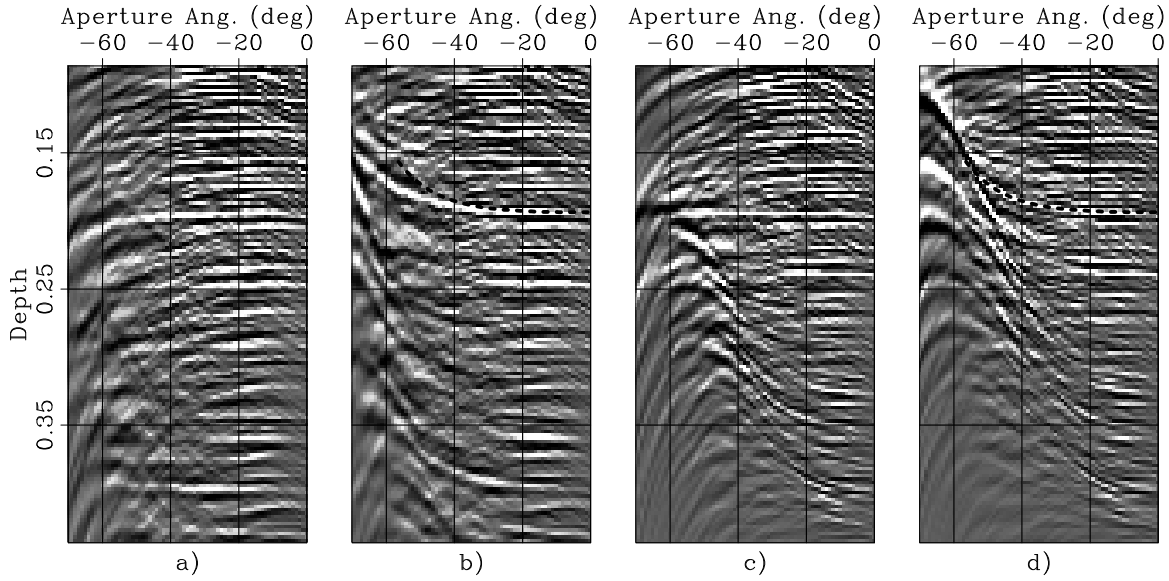

Figure 12: ADCIGs taken at the surface location of 3,725 meters and with the layer below the sea floor being: a) anisotropic and heterogeneous, b) isotropic and heterogeneous, c) anisotropic and homogeneous ($V_V = 1,750$ m/s, $\epsilon = 0.11$, $\delta = 0.04$, and $\eta = .065$), d) isotropic and homogeneous ($V_V = 1,750$ m/s). The RMO curve that is superimposed onto panels b) and d) is computed using equations 24–26. biondo2-Quad-Aniso-shallow-overn [CR]

in Figure 12d. In contrast, the computed RMO function overestimates the moveout in the ADCIG obtained by migrating the data using the original isotropic model (Figure 12b). The cause of this discrepancy is the ray bending induced by the vertical gradient in the original heterogeneous model. Because of ray bending the events propagate more vertically, and thus more slowly, in the heterogeneous medium than in the homogeneous one. In cases when explicit raytracing though the background velocity is necessary to compute the RMO function, equation 27 provides the necessary link between the traveltime perturbations accumulated along the rays and the depth perturbations measured in the ADCIGs.

The ADCIGs shown in Figure 13 display a behavior similar to the ones shown in Figure 12. Since the reflection of interest is now deep, the half-space below the sea floor is characterized by higher average parameters than for the shallow reflection; that is: $V_V = 2,000$ m/s, $\epsilon = 0.143$, $\delta = 0.045$, and $\eta = .09$. As before, the reflection of interest in ADCIG migrated using these parameters (Figure 13c) is flat, whereas the same reflection in the ADCIG migrated with isotropic migration with the same vertical velocity ($V_V = 2,000$ m/s) is smiling upward (Figure 13d). As before, the RMO curve computed using equations 24–26 perfectly overlaps the event in the ADCIG shown in Figure 13d, whereas it overestimates the moveout in the ADCIG obtained by migrating the data using the original isotropic model (Figure 13b).

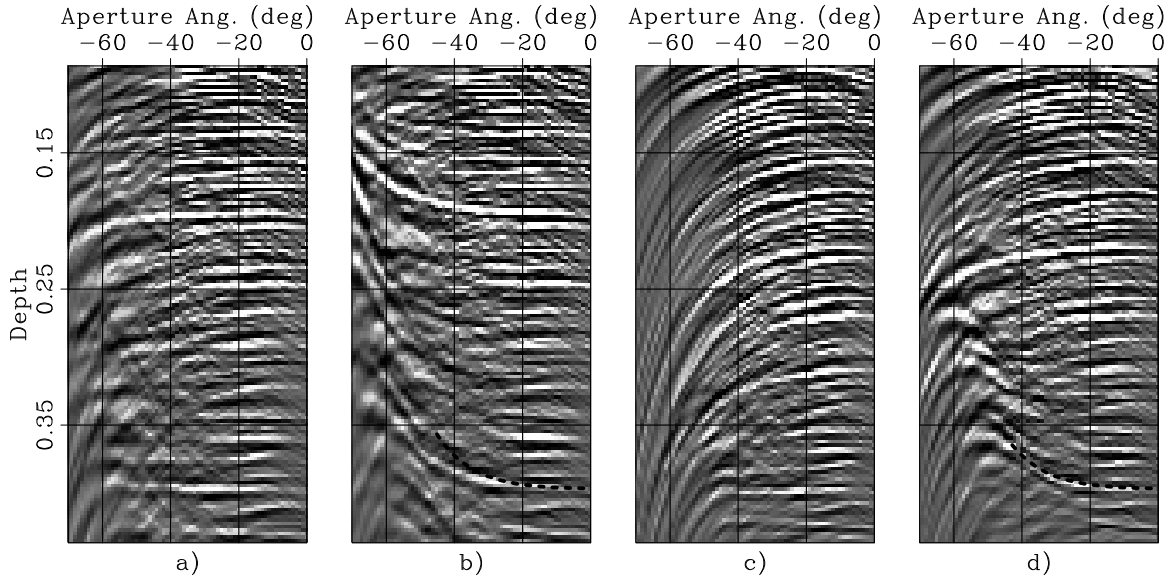

Figure 13: ADCIGs taken at the surface location of 3,725 meters and with the layer below the sea floor being: a) anisotropic and heterogeneous, b) isotropic and heterogeneous, c) anisotropic and homogeneous ($V_V = 2{,}000$ m/s, $\epsilon = 0.143$, $\delta = 0.045$, and $\eta = .09$), d) isotropic and homogeneous ($V_V = 2{,}000$ m/s). The RMO curve that is superimposed onto panels b) and d) is computed using equations 24–26. biondo2-Quad-Aniso-deep-overn [CR]

CONCLUSIONS

The methodology presented in this paper enables the use of ADCIGs to iteratively estimate anisotropic velocity parameters in conjunction with anisotropic wavefield-continuation migration. This advancement should enable the performance of MVA in areas where the overburden is both anisotropic and complex to require anisotropic wavefield-continuation migration.

The linearized analysis of depth perturbations in ADCIGs obtained by anisotropic migration shows that the RMO function observed when the migration velocity is inaccurate is a function of both the phase aperture angle and the group aperture angle. The synthetic-data examples show that the linearized expression of the RMO function accurately predicts the actual RMO function measured after wavefield migration.

The real data results confirm the accuracy of the theory developed in this paper. The RMO curves predicted by the theory match extremely well the RMO functions observed in the ADCIG migrated according to the assumptions underlying the theory. We observe fairly large differences in RMO functions observed between the ADCIGs computed assuming an isotropic homogeneous half-space hanging from the sea floor and the ADCIGs computed assuming an isotropic heterogeneous model. These discrepancies demonstrate the sensitivity of the RMO analysis to the accuracy with which the background velocity predicts the actual ray bending. This sensitivity is higher for anisotropic media because of the velocity dependence on the

propagation angle, suggesting that a tomographic MVA might be even more necessary for anisotropic media than for isotropic ones.

Tomographic updating of the anisotropic parameters from ADCIGs can be based on the same fundamental concepts used to derive the RMO functions presented and tested in this paper. I therefore derive the linearized relationship between depth errors measured in ADCIGs and traveltime errors accumulated along the wavepaths. This relationship should lead to the development of anisotropic MVA methods based on tomographic velocity-updating procedures.

ACKNOWLEDGMENTS

I would like to thank the ExxonMobil Exploration Company for making the Gulf of Mexico data set used in this paper data available to SEP through the generous efforts of Ruth Gonzalez and Joe Reilly. The anisotropic parameters cube were kindly shared with us by Laura Bear and Jerry Krebs, also at ExxonMobil.

REFERENCES

Bear, L., Dickens, T., and Traynin, P., 2003, Incorporating nonseismic information for improved positioning with anisotropic PSDM: 73rd Ann. Internat. Meeting, Soc. of Expl. Geophys., Expanded Abstracts, 949–952.

Biondi, B., and Sava, P., 1999, Wave-equation migration velocity analysis: 69th Ann. Internat. Meeting, Soc. of Expl. Geophys., Expanded Abstracts, 1723–1726.

Biondi, B., and Symes, W. W., 2003, Angle-domain common-image gathers for migration velocity analysis by wavefield-continuation imaging: Geophysics, **69**, 1283–1298.

Biondi, B., and Tisserant, T., 2004, 3-D angle-domain common-image gathers for migration velocity analysis: Geophisical Prospecting, **52**, 575–591.

Biondi, B., 2005, Angle-domain common image gathers for anisotropic migration: SEP–**123**.

Clapp, R., and Biondi, B., 2000, Tau domain migration velocity analysis using angle CRP gathers and geologic constrains: 70th Ann. Internat. Meeting, Soc. of Expl. Geophys., Expanded Abstracts, 926–929.

Dellinger, J., and Muir, F., 1985, Two domains of anisotropy: SEP–**44**, 59–62.

Fowler, P., 2003, Practical VTI approximations: a systematic anatomy: Journal of Applied Geophysics, **69**, 347–367.

Krebs, J., Bear, L., and Liu, J., 2003, Integrated velocity model estimation for accurate imaging: 73rd Ann. Internat. Meeting, Soc. of Expl. Geophys., Expanded Abstracts, 2084–2087.

Sarkar, D., and Tsvankin, I., 2003, Analysis of image gathers in factorized vti media: Geophysics, **68**, 2016–2025.

Sarkar, D., and Tsvankin, I., 2004a, Anisotropic migration velocity analysis: Application to a data set from West Africa: 74th Ann. Internat. Meeting, Soc. of Expl. Geophys., Expanded Abstracts, 2399–2402.

Sarkar, D., and Tsvankin, I., 2004b, Migration velocity analysis in factorized vti media: Geophysics, **69**, 708–718.

Tsvankin, I., 2001, Seismic signatures and analysis of reflection data in anisotropic media: Elsevier Science.

APPENDIX A

PHASE AND GROUP ANGLES AND VELOCITIES

In anisotropic wave propagation the phase angles and velocities are different from the group angles and velocities. In this appendix I briefly review the concepts of phase and group angles and velocities and the relationships between these physical quantities.

The transformation from phase velocity $\widetilde{V}$ to group velocity V is conventionally defined as the following (Tsvankin, 2001):

$$V = \sqrt{\widetilde{V}^2 + \left(\frac{d\widetilde{V}}{d\widetilde{\theta}}\right)}, \tag{A-1}$$

where $\widetilde{\theta}$ is the phase propagation angle. The associated transformation from phase angles to group angles θ is defined as:

$$\tan\theta = \frac{\tan\widetilde{\theta} + \frac{1}{\widetilde{V}}\frac{d\widetilde{V}}{d\theta}}{1 - \frac{1}{\widetilde{V}}\frac{d\widetilde{V}}{d\widetilde{\theta}}\tan\widetilde{\theta}}. \tag{A-2}$$

Dellinger and Muir (1985) propose, and heuristically motivate, the following symmetric relations for the inverse transforms:

$$\widetilde{S} = \sqrt{S^2 + \left(\frac{dS}{d\theta}\right)}, \tag{A-3}$$

where $\widetilde{S}$ and S are respectively the phase slowness and the group slowness, and

$$\tan\widetilde{\theta} = \frac{\tan\theta + \frac{1}{S}\frac{dS}{d\theta}}{1 - \frac{1}{S}\frac{dS}{d\theta}\tan\theta}. \tag{A-4}$$

I use the heuristic relation in equation A-4 to derive some of the analytical results presented in this paper. Furthermore, I use all the above relationships to compute the kinematic numerical results presented in this paper.

APPENDIX B

INDEPENDENCE OF DEPTH PERTURBATIONS FROM ANGLE PERTURBATIONS

In this appendix I demonstrate that the terms in equation 13 multiplying the partial derivatives with respect to the angles; that is, $\partial\gamma/\partial\rho_i$ and $\partial\widetilde{\gamma}/\partial\rho_i$, are zero when evaluated at the point when the events are correctly migrated at zero subsurface offset. We are interested in estimating the RMO function measured for an incorrect velocity. That RMO function can be seen as a perturbation around the image obtained with the correct velocity.

After simple evaluation of partial derivatives the term multiplying $\partial\gamma/\partial\rho_i$ in equation 13 can be written as the following:

$$\begin{aligned}\left(\frac{\partial z_\gamma}{\partial L}\frac{\partial L}{\partial S(\gamma)}\frac{\partial S(\gamma)}{\partial\gamma}+\frac{\partial z_\gamma}{\partial\gamma}\right) &= -\frac{z_\xi\left(\cos\gamma+\sin\gamma\tan\widetilde{\gamma}\right)}{S(\gamma)\cos\gamma}\frac{\partial S(\gamma)}{\partial\gamma}-L\left(\sin\gamma-\cos\gamma\tan\widetilde{\gamma}\right)\\ &= -z_\xi\left[\left(1+\tan\gamma\tan\widetilde{\gamma}\right)\frac{\partial S(\gamma)}{\partial\gamma}+\tan\gamma-\tan\widetilde{\gamma}\right], \qquad \text{(B-1)}\end{aligned}$$

that can be easily demonstrated to be equal to zero after substitution of the relationship between phase angles and group angles presented in equation A-4.

The term multiplying $\partial\widetilde{\gamma}/\partial\rho_i$ is equal to

$$\frac{\partial z}{\partial\widetilde{\gamma}} = -h_\xi\frac{1}{\cos^2\widetilde{\gamma}}, \qquad \text{(B-2)}$$

which is obviously equal to zero when the subsurface offset is zero, the point around which we are interested in expanding the RMO function.

APPENDIX C

DERIVATIVES OF VTI SLOWNESS FUNCTION WITH RESPECT TO THE PERTURBATION PARAMETERS

In this Appendix I present the analytical expressions for the derivatives of the group slowness function with respect to the velocity-perturbation parameters $\left(\rho_{V_V},\rho_{V_H},\rho_{V_N}\right)$. These derivatives depend on the particular form chosen to approximate the slowness function. In this paper I use following approximation of the VTI slowness function (Fowler, 2003):

$$\begin{aligned}S^2_{\text{VTI}}(\theta) &= \frac{{S_V}^2\cos^2\theta+{S_H}^2\sin^2\theta+\sqrt{\left({S_V}^2\cos^2\theta+{S_H}^2\sin^2\theta\right)^2+{S_V}^2\left({S_N}^2-{S_H}^2\right)\sin^2 2\theta}}{2}\\ &= \frac{S^2_{\text{Ell}}(\theta)+\sqrt{S^4_{\text{Ell}}(\theta)+{S_V}^2\left({S_N}^2-{S_H}^2\right)\sin^2 2\theta}}{2}, \qquad \text{(C-1)}\end{aligned}$$

where

$$S_{\mathrm{Ell}}^2(\theta) = {S_V}^2 \cos^2\theta + {S_H}^2 \sin^2\theta \tag{C-2}$$

is the elliptical component.

The derivatives are then written as:

$$\left.\frac{\partial S_{\mathrm{VTI}}(\theta)}{\partial \rho_{V_V}}\right|_{\rho=\mathbf{1}} = \frac{S_{\mathrm{Ell}}(\theta)}{2S_{\mathrm{VTI}}(\theta)}\frac{\partial S_{\mathrm{Ell}}(\theta)}{\partial \rho_{V_V}} + \frac{2\frac{\partial S_{\mathrm{Ell}}(\theta)}{\partial \rho_{V_V}} S_{\mathrm{Ell}}^3(\theta) - {S_V}^2\left({S_N}^2 - {S_H}^2\right)\sin^2 2\theta}{4S_{\mathrm{VTI}}(\theta)\sqrt{S_{\mathrm{Ell}}^4(\theta) + {S_V}^2\left({S_N}^2 - {S_H}^2\right)\sin^2 2\theta}}, \tag{C-3}$$

$$\left.\frac{\partial S_{\mathrm{VTI}}(\theta)}{\partial \rho_{V_H}}\right|_{\rho=\mathbf{1}} = \frac{S_{\mathrm{Ell}}(\theta)}{2S_{\mathrm{VTI}}(\theta)}\frac{\partial S_{\mathrm{Ell}}(\theta)}{\partial \rho_{V_H}} + \frac{2\frac{\partial S_{\mathrm{Ell}}(\theta)}{\partial \rho_{V_H}} S_{\mathrm{Ell}}^3(\theta) + {S_V}^2{S_H}^2\sin^2 2\theta}{4S_{\mathrm{VTI}}(\theta)\sqrt{S_{\mathrm{Ell}}^4(\theta) + {S_V}^2\left({S_N}^2 - {S_H}^2\right)\sin^2 2\theta}}, \tag{C-4}$$

$$\left.\frac{\partial S_{\mathrm{VTI}}(\theta)}{\partial \rho_{V_N}}\right|_{\rho=\mathbf{1}} = \frac{-{S_V}^2{S_N}^2\sin^2 2\theta}{4S_{\mathrm{VTI}}(\theta)\sqrt{S_{\mathrm{Ell}}^4(\theta) + {S_V}^2\left({S_N}^2 - {S_H}^2\right)\sin^2 2\theta}}, \tag{C-5}$$

where the derivatives of the elliptical component with respect to ρ_{V_V} and ρ_{V_H} are:

$$\left.\frac{\partial S_{\mathrm{Ell}}(\theta)}{\partial \rho_{V_V}}\right|_{\rho=\mathbf{1}} = \frac{-{S_V}^2\cos^2\theta}{S_{\mathrm{Ell}}(\theta)} \tag{C-6}$$

$$\left.\frac{\partial S_{\mathrm{Ell}}(\theta)}{\partial \rho_{V_H}}\right|_{\rho=\mathbf{1}} = \frac{-{S_H}^2\sin^2\theta}{S_{\mathrm{Ell}}(\theta)}. \tag{C-7}$$